*remote sensing*

MDPI

*Article*

# A Semianalytic Monte Carlo Simulator for Spaceborne Oceanic Lidar: Framework and Preliminary Results

**Qun Liu [1], Xiaoyu Cui [1], Cédric Jamet [2], Xiaolei Zhu [3], Zhihua Mao [4], Peng Chen [4], Jian Bai [1] and Dong Liu [1,5,*]**

1 State Key Laboratory of Modern Optical Instrumentation, College of Optical Science and Engineering, Ningbo Research Institute, Zhejiang University, Hangzhou 310027, China; liuqun@zju.edu.cn (Q.L.); xycui@zju.edu.cn (X.C.); bai@zju.edu.cn (J.B.)
2 University Littoral Cote d'Opale, University Lille, CNRS, UMR 8187, LOG, Laboratoire d'Océanologie et de Géosciences, 62930 Wimereux, France; cedric.jamet@univ-littoral.fr
3 Shanghai Institute of Optics and Fine Mechanics, Chinese Academy of Sciences, Shanghai 201800, China; xlzhu@siom.ac.cn
4 State Key Laboratory of Satellite Ocean Environment Dynamics, Second Institute of Oceanography, Ministry of Natural Resources, Hangzhou 310012, China; mao@sio.org.cn (Z.M.); chenp@sio.org.cn (P.C.)
5 International Research Center for Advanced Photonics, Zhejiang University, Hangzhou 310027, China
* Correspondence: liudongopt@zju.edu.cn; Tel.: +86-135-7578-8748

Received: 27 July 2020; Accepted: 26 August 2020; Published: 31 August 2020


**Abstract:** Spaceborne lidar (light detection and ranging) is a very promising tool for the optical properties of global atmosphere and ocean detection. Although some studies have shown spaceborne lidar's potential in ocean application, there is no spaceborne lidar specifically designed for ocean studies at present. In order to investigate the detection mechanism of the spaceborne lidar and analyze its detection performance, a spaceborne oceanic lidar simulator is established based on the semianalytic Monte Carlo (MC) method. The basic principle, the main framework, and the preliminary results of the simulator are presented. The whole process of the laser emitting, transmitting, and receiving is executed by the simulator with specific atmosphere–ocean optical properties and lidar system parameters. It is the first spaceborne oceanic lidar simulator for both atmosphere and ocean. The abilities of this simulator to characterize the effect of multiple scattering on the lidar signals of different aerosols, clouds, and seawaters with different scattering phase functions are presented. Some of the results of this simulator are verified by the lidar equation. It is confirmed that the simulator is beneficial to study the principle of spaceborne oceanic lidar and it can help develop a high-precision retrieval algorithm for the inherent optical properties (IOPs) of seawater.

**Keywords:** spaceborne oceanic lidar; semianalytical Monte Carlo; lidar signal; atmosphere-ocean

## 1. Introduction

The marine ecosystems are extremely complex and play an essential role in the biosphere. The phytoplankton is at the basis of the marine food web [1], and their annual net photosynthetic carbon fixation is nearly equivalent to that of all terrestrial plants [2,3]. The utilization and protection of the ocean is crucial to the sustainable development of human society. The ocean has been globally monitored by the spaceborne sensors for the past several decades.

Passive remote sensing of Ocean Color Radiometry (OCR) has provided a global view of the concentration of phytoplankton total suspended matter, colored dissolved organic matter (CDOM), and so on [4–6]. The performance of OCR spaceborne sensors has gradually improved since the

launch of the Coastal Zone Color Sensor (in 1978 as a proof-of-concept), which has benefitted from an increased number of detection wavelength bands and improved retrieval algorithms [5]. We now have access to a continuous record of OCR since 1997 thanks to a series of satellites: Sea-Viewing Wide Field-of-View Sensor (SeaWiFS), Moderate Resolution Imaging Spectroradiometer (MODIS), Medium Resolution Imaging Spectrometer (MERIS, 2002–2012), Visible Infrared Imaging Radiometer Suite (VIIRS), Ocean and Land Color Imager (OLCI), and so on. However, the observation performance of ocean color measurements should be improved in some aspects such as the retrieval methods, which are highly sensitive to the atmospheric correction errors; the expansion of the temporal and spatial range of observation; the depth-resolved information of the subsurface ocean [7].

Lidar (light detection and ranging) is an active remote sensing technique that can provide vertical distribution information of the subsurface ocean [8,9] and has been applied in the observation of the optical properties of plankton [10,11], fish schools [12], air bubbles [13], and internal waves [14]. These applications are all based on shipborne or airborne lidar systems [15,16]. Up to now, there is no spaceborne lidar specifically designed for ocean applications. The Cloud-Aerosol Lidar with Orthogonal Polarization (CALIOP) was primarily designed for atmospheric research at the early stage of its mission [17]. Hu et al. extended the application of CALIOP data from the atmosphere to the ocean, demonstrating the possibility of spaceborne lidar to obtain global ocean surface optical parameters [18]. However, due to the limited vertical resolution (22.5 m in the ocean), it cannot provide depth-resolved estimates of the bio-optical properties of the seawater [19]. Recently, many countries have proposed spaceborne oceanic lidar programs. The Ice, Cloud, and Land Elevation Satellite-2 (ICESat-2) launched in 2018 has greatly improved the altimetry technology and accuracy based on the ICESat technology [20]. The basic scientific aims of the ICESat-2 mission are to measure sea ice freeboard and ice sheet elevation continuously to determine their changes at scales from outlet glaciers to the entire ice sheet, and from 10 s of meters to the entire polar oceans for the sea ice freeboard [20]. The Atmospheric Dynamics Mission ADM-Aeolus was launched in 2018 and makes direct measurements of global wind fields. The aim is to provide global observations of wind profiles with a vertical resolution that will satisfy the requirements of the World Meteorological Organization. The only payload is the Atmospheric Laser Doppler Instrument (ALADIN), which is a direct detection Doppler lidar operating in the UV [21,22]. China has carried out pre-research work on spaceborne oceanic lidar in its national key research and development program and put forward the concept design of the "Guanlan" Science Mission with an oceanic lidar payload [23]. Since the development of spaceborne oceanic lidar is a very big project, it is necessary to build a comprehensive and accurate lidar return signal simulator to study the lidar detection mechanism in the early development stage to ensure the feasibility and availability of the lidar system. There are some lidar simulators in the literature [24–26], but they are not designed for spaceborne oceanic lidar.

There are several algorithms to characterize the process of laser radiation transmission in the atmosphere and ocean. When the optical depth of the atmosphere and seawater is low, the lidar signal can be expressed accurately by the single scattering theory [27]. However, multiple scattering can cause temporal and spatial expansion of the laser beam, which makes the backscattered lidar signal more complex [28]. The analytical lidar equation considering multiple scattering effects has been proposed, but there are calculation errors resulting from the application of a quasi-single small-angle (QSSA) approximation and some other approximations [29–31].

The Monte Carlo (MC) method is a convenient alternative for solving the complicated radiative transfer equation (RTE) in optical remote sensing [32]. It has been proved that the data obtained by MC simulation is consistent with that of shipborne lidar experiments [33]. The cost of MC simulation is lower, which only needs some computing time and computer memory, and it can provide good preliminary support for field experiments. However, although the classical MC method can give a good result, the low computation speed drives us to improve the efficiency of calculation in the process of constructing the simulator.

In this paper, a spaceborne oceanic lidar simulator is built using a semianalytical Monte Carlo method, which can obtain the lidar returns from different atmosphere and ocean conditions. This is the first spaceborne oceanic lidar simulator that can be used to calculate the optical properties and the lidar signals of both atmosphere and ocean simultaneously. The simulator is helpful to explore the shapes of spaceborne lidar returns as a function of the seawater optical properties, to analyze the effects of multiple scattering, and to pave the way for the estimation of seawater inherent optical properties (IOPs), (i.e., the particulate back-scattering coefficient [4]). Furthermore, more application related to the ecology such as the study of polar phytoplankton biomass [34] and measurements of global ocean carbon sticks [35] can be done with accurate lidar data. The principle and method of the simulator is in Section 2. In Section 3, we use this simulator to obtain lidar returns from various ocean conditions, such as different types of scattering phase functions and the inhomogeneity of seawaters. Discussions on the preliminary results of the simulator are given in Section 4. A conclusion of this paper along with an outlook of possible improvements are outlined in the last section.

## 2. Principle and Methods

### 2.1. Principle of the Spaceborne Oceanic Lidar

The detection principle of the spaceborne oceanic lidar is given in Figure 1. The lidar system is mainly composed of the transmitting and the receiving systems. The transmitting system emits a pulsed laser into the atmosphere and ocean. Then, the laser pulse goes through absorption and scattering effects by aerosols and clouds in the atmosphere and by water molecules, CDOM, total suspended matter (TSM), and phytoplankton in ocean, as well as the refraction and reflection of the air–ocean interface. Finally, the detector in the receiving system gets the lidar return signals containing optical information of the atmosphere and ocean. The lidar return signal can be given by the lidar equation [19].

$$P(z) = P_0 K \frac{v\tau}{2n} \frac{A T_a^2 T_s^2}{(nH+z)^2} \beta_\pi(z) \exp(-2\int_0^z k_{\text{lidar}}(z\prime)dz\prime) \quad (1)$$

where $P(z)$ is the power received by the detector from depth $z$, $P_0$ is the transmitted power, $K$ is the constant of the lidar system instrument, $v$ is the speed of light in vacuum, $\tau$ is the pulse width, $n$ is the refractive index of seawater, $T_s$ is the Fresnel transmittance of the air–ocean interface, $A$ is the area of the detector, $H$ is the altitude of the lidar above the sea surface, $\beta_\pi$ is the volume-scattering coefficient at a scattering angle of $\pi$ rad, $k_{\text{lidar}}$ is the effective attenuation coefficient, and $T_a$ is the transmission through the atmosphere, which can be expressed as

$$T_a = \exp(-2\int_0^H \alpha_a(z\prime)dz\prime) \quad (2)$$

where $\alpha_a$ is the extinction coefficient of the atmosphere. The lidar equation reveals that the power is related to the hardware parameters of lidar, the height of the lidar, as well as the optical properties of seawater. The simulator is designed to solve the lidar equation exactly. $\beta_\pi$ and $k_{\text{lidar}}$ are essential parameters for retrieving the optical properties of seawater. As is explained in reference [36], if the field of view (FOV) of the lidar receiver is large enough, the backscattering signal from the seawater is attenuated at a rate determined by the absorption coefficient. The radius of the receiving footprint on the sea surface from the spaceborne lidar system is usually tens of meters; that means that the FOV is large enough, so $k_{\text{lidar}}$ is close to the absorption coefficient $a$. Moreover, the scattering phase function described in Section 2.3 is also an important parameter. The particulate backscattering coefficient $b_{bp}$ can be obtained from the volume scattering function of particle $\beta_p(\theta)$ by using Equation (3), which is a key biogeochemical parameter [35].

$$b_{bp} = 2\pi \int_{\pi/2}^{\pi} \beta_p(\theta) \sin\theta d\theta \quad (3)$$

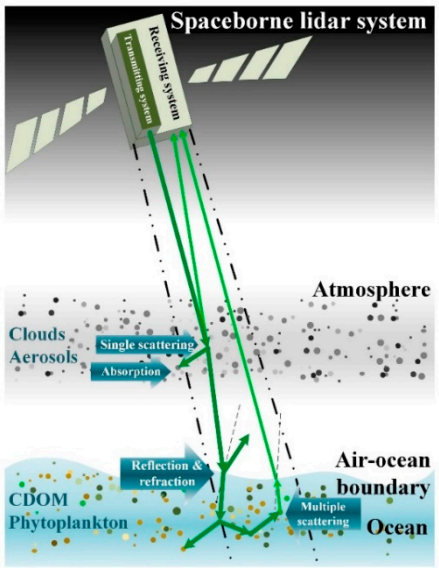


**Figure 1.** Simplified diagram of the detection principle of spaceborne oceanic light detection and ranging (lidar).

### 2.2. Simulation Method

The traditional MC method is very time-consuming. To improve simulation efficiency, several methods have been applied including a semianalytic MC algorithm, photon weight method, and multithreading operation method [19,26].

Based on the photon weight method, the semianalytic MC algorithm combines stochastic simulation and an analytical algorithm to calculate the expected proportion of the photon packet [26], which can return to the detector without further interaction. As shown in Figure 2, the photon packet moves from point O to point B in the direction $\vec{\varepsilon}'$. The expected value of the collected photon packet can be described as

$$E = \frac{p(\theta)}{4\pi}\Delta\Omega \exp(-\int_0^d c(z)\mathrm{d}z)T_s T_a \quad (4)$$

where $p(\theta)$ is the scattering phase function, which represents the part of the photon packet scattered into an element of solid angle $\Delta\Omega$ about direction $\theta$ [26].

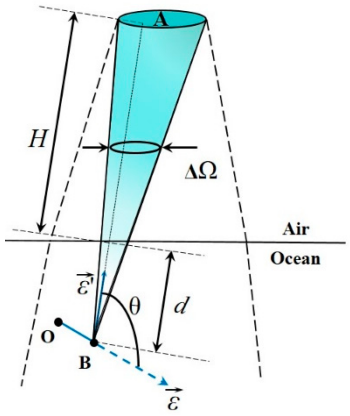


**Figure 2.** The principle of the semianalytic Monte Carlo (MC) method.

The flow chart of the simulator is shown in Figure 3. To run the semianalytic MC simulation process with the simulator, lidar parameters (laser pulse energy, pulse width, height of the lidar, divergence angle of laser, etc.), environment parameters (absorption and scattering coefficients and

phase functions of atmosphere and seawater, etc.) and output file parameters (vertical resolution of atmosphere and seawater, path of output file, etc.) need to be set.

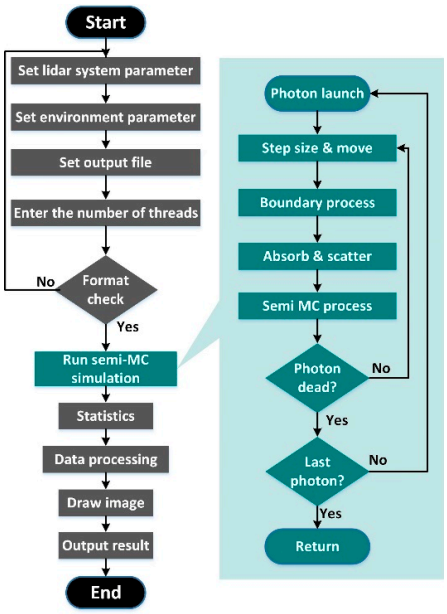


**Figure 3.** Flow chart of spaceborne lidar simulator.

In the semianalytical MC simulation, the Cartesian coordinates are used to describe the position and direction of the photon. The position of the photon is represented as $(x, y, z)$, and the initial position is (0, 0, 0). The direction of the photon is represented by the cosine of the angle between the direction of the photon and the coordinate axes ($u_x$, $u_y$, $u_z$). The schematic diagram of the photon scattering direction is shown in Figure 4. The origin direction is $\vec{OA}$, and the new direction after scattering is $\vec{OB}$. There are two angles that determine the scattering direction of the photon, including the scattering angle $\varphi$ and the azimuth angle $\theta$. The scattering angle represents the angle between the new direction after scattering and the previous original direction, $\theta \in (0, \pi)$. The azimuth angle represents the angle at which the photon is projected on the plane with respect to a reference direction, $\varphi \in [0, 2\pi)$. The step size $s$ is defined as the integration of the attenuation coefficient $c$ over the photon pathway, which is calculated by $s = -\ln(1-\xi)/c$, where $\xi$ is a random number uniformly distributed in [0,1]. The position is transformed from $(x, y, z)$ to a new one $(x', y', z')$ when the photon moved. The conversion equation is given by

$$x' = x + u_x s;\ y' = y + u_y s;\ z' = z + u_z s. \tag{5}$$

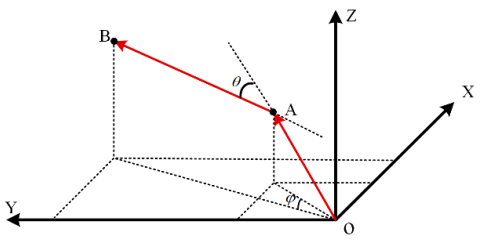


**Figure 4.** The schematic diagram of the photon scattering direction.

When the photon interacts with particles, the photon weight is updated by $W' = W \times \omega_0$, where $W$ is the weight of the photon packet before collision and $\omega_0$ is the single scattering albedo ($\omega_0 = b/c$). The reflectance of the sea surface can be calculated according to the Fresnel formula if the sea surface

is considered as flat. If the random number is less than the reflectance, the photon will be reflected; otherwise, it will be refracted into the seawater according to the refraction law.

### *2.3. Scattering Phase Function Models*

The backscattered lidar signals from the atmosphere and ocean are closely related to their scattering characteristics. The scattering coefficient and the scattering phase function are important to represent the scattering characteristics of the media. The scattering phase function is the ratio of the volume scattering function (VSF) to the scattering coefficient, which specifies the angular dependence of the scattering without regard for its magnitude [37]. The phase functions of atmosphere and seawater included in this simulator are introduced below.

#### 2.3.1. Scattering Phase Function of the Atmosphere

The phase function for atmospheric molecules is approximated by Rayleigh scattering, which can be given by [38]

$$\widetilde{\beta}_{\mathrm{m}}(\theta) = 3(1 + p\cos^2\theta)/[4\pi(3 + p)] \tag{6}$$

with the polarization parameter $p$ = 1. The phase function of the clouds and aerosols in the atmosphere can be calculated with Mie theory [39], as the radius distribution and optical properties are given. It is expressed as

$$\widetilde{\beta}_{\mathrm{p}}(\theta) = \frac{2\pi}{k^2 b}\int_{r_1}^{r_2}[i_1(r,\theta) + i_2(r,\theta)]\frac{dN(r)}{dr}dr \tag{7}$$

where $b = \int_{r_1}^{r_2}\sigma(r)\frac{\mathrm{d}N(r)}{\mathrm{d}r}\mathrm{d}r$, and $\sigma(r)$ is the scattering cross-section of the particle. $i_1$ and $i_2$ are the parallel and vertical components of scattered light intensity, respectively. $\mathrm{d}N(r)/\mathrm{d}r$ is the distribution function of the particle radius.

The software package optical properties of aerosols and clouds (OPAC) [40] provides the microphysical and optical properties of 6 water clouds, 3 ice clouds, and 10 aerosol components, which are included in this simulator as typical and available cases. According to OPAC [40], Gamma and lognormal distributions are two main size distribution functions for particles in atmosphere. The equation of the Gamma distribution is [40]

$$\mathrm{d}N(r)/\mathrm{d}r = Nar^{\alpha}\exp(-Br^{\gamma}) \tag{8}$$

where $B = \alpha/\gamma r_{\mathrm{mod}}^{\gamma}$, $N$ is the total number density in particles per cubic centimeter, $r_{\mathrm{mod}}$ is the mode radius in micrometers, $\alpha$ and $\gamma$ are two constants that describe the slope of the size distribution, and $a$ is the normalization constant. The equation of lognormal distribution is

$$\frac{\mathrm{d}N(r)}{\mathrm{d}r} = \frac{N}{\sqrt{2\pi}r\log\mu\ln 10}\exp[\frac{1}{2}(\frac{\log r - \log r_{\mathrm{mod}}}{\log\mu})^2] \tag{9}$$

where $b_{\mathrm{m}}$ and $b_{\mathrm{p}}$ are the scattering coefficients of atmospheric molecules and particles, respectively, and $b_{\mathrm{atm}} = b_{\mathrm{m}} + b_{\mathrm{p}}$.

#### 2.3.2. Scattering Phase Function of Seawater

The scattering phase function of seawater influences the shape of the lidar return signal. Limited by the measurement technology, the scattering phase function of seawater at small and large scattering angles has not been accurately measured. The typical measured phase function is the averaged-particle phase function derived from three measurements of VSF of the Bahama Islands, San Pedro Channel, and San Diego Harbor by Petzold (Petzold phase function for short) [41]. The Petzold phase function is given in form of discrete data and can be used by the lookup table method in MC simulation. At present, this simulator includes the averaged Petzold phase function, One-Term Henyey–Greenstein (OTHG)

phase function [42], two-term Henyey–Greenstein (TTHG) phase function [43,44] and Fournier–Forand (FF) phase function [45]. Meanwhile, the user-defined phase function is also accepted, allowing the user to make any possible modification to the current ones or calculating with their own one. The OTHG phase function is a one-parameter function that is widely used in ocean optics because of its mathematical simplicity: [46]

$$\widetilde{\beta}_{\mathrm{OTHG}}(\theta) = \frac{1}{4\pi}\frac{1-g^2}{(1+g^2-2g\cos\theta)^{3/2}} \tag{10}$$

where $g$ is asymmetry factor, ranging from −1 to 1 [46].

The OTHG phase function gives a poor description of the particulate phase functions at large and small scattering angles [43]. Therefore, a weighted sum of the OTHG phase function, which is called the TTHG phase function, is proposed [43,44]:

$$\widetilde{\beta}_{\mathrm{TTHG}}(\theta) = \alpha\widetilde{\beta}_{\mathrm{OTHG}}(\theta, g_1) + (1-\alpha)\widetilde{\beta}_{\mathrm{OTHG}}(\theta, g_2). \tag{11}$$

The parameter $g_1$ is given a value near 1, which makes the TTHG phase function increase more strongly at small $\theta$ than does the OTHG phase function. The $g_2$ parameter is given a negative value, which makes the TTHG increase with the scattering angle $\theta$ approaching $\pi$ rad. The expression for parameters $g_2$ and $\alpha$ can be given as functions of $g_1$ [44]:

$$\begin{cases} g_2 = -0.30614 + 1.0006g_1 - 0.01826g_1^2 + 0.03644g_1^3 \\ \alpha = \frac{g_2(1+g_2)}{((g_1+g_2)(1+g_2-g_1)} \end{cases}. \tag{12}$$

The FF phase function is derived from a collection of Mie scattering with a Junge particle size distribution [45], which is based on the anomalous diffraction approximation [47]

$$\widetilde{\beta}_{\mathrm{FF}}(\theta) = \frac{1}{4\pi(1-\delta)^2\delta^v}[v(1-\delta) - (1-\delta^v) + [\delta(1-\delta^v) - v(1-\delta)]\sin^{-2}(\theta/2)] + \frac{1-\delta_{180^\circ}^v}{16\pi(\delta_{180^\circ}-1)\delta_{180^\circ}^v}(3\cos^2\theta - 1) \tag{13}$$

where $v = (3-\mu)/2$, $\delta = 4/\left[3(n-1)^2\right]\sin^2(\theta/2)$, $n$ is the true refractive index of particles, $\mu$ is the slope of hyperbolic distribution, and $\delta_{180^\circ}$ is the value of $\delta$ at $\theta = 180^\circ$.

The particle backscattering fraction $B_{\mathrm{p}}$ represents the probability that a photon will be scattered through an angle ≥ 90°, which is given by $B_{\mathrm{p}} = b_{\mathrm{bp}}/b_{\mathrm{p}}$. The subscript p represents particles, and $b_{\mathrm{b}}$ is the backscatter coefficient, which is the integral of the VSF over the hemisphere of the backscattering directions. These mentioned phase functions are plotted in Figure 5 with $B_{\mathrm{p}} = 0.0183$, which is consistent with that of the Petzold phase function [46]. These seawater phase functions are all strongly peaked in the forward direction. In the backward scattering direction, both FF and OTHG are similar to Petzold. However, the TTHG phase function has a characteristic of high backscattering and low forward scattering compared to the other three phase functions according to Figure 5.

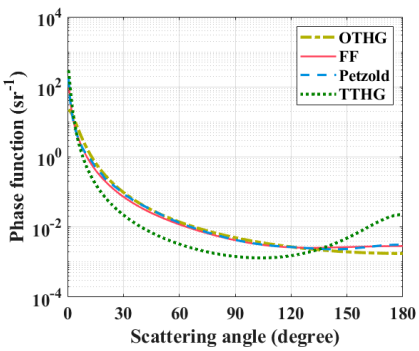


**Figure 5.** Scattering phase functions of seawater in the simulator.

## 3. Results

Some preliminary simulation results are presented here to demonstrate the performance of the simulator. The parameters of the elastic lidar system used in the simulations in this paper are given in Table 1. The air–ocean interface in this simulator is assumed to be flat, and the strong reflection from the surface is ignored, because that the lidar usually operates at an oblique incidence for ocean observation [48,49]. In order to save the simulation time and ensure a low level of standard deviation of the statistical results [19], all the simulations in this paper are executed with $10^8$ photon packets.

**Table 1.** Parameters of the spaceborne lidar system.

| Parameter | Value |
|---|---|
| Laser wavelength (nm) | 532 |
| Power of the laser (mJ) | 100 |
| Pulse width (nm) | 2 |
| Divergence angle (mrad) | 0.1 |
| Lidar height (km) | 700 |
| Field of view (mrad) | 0.15 |
| Telescope diameter (m) | 1.0 |

### 3.1. Results of Atmosphere–Ocean Simulation

In order to give an overall view of the performance of this simulator, firstly, we simulate the spaceborne lidar return signal from the atmosphere and ocean. The atmosphere within 30 km (atmosphere above 30 km is clean air) is equally divided into 300 horizontal layers. The Rayleigh-scattering theory is adopted to calculate the optical properties of air molecules [50]. Two typical atmosphere cases are shown in Figure 6, where the blue dashed line is for aerosol and the red solid line is for cloud.

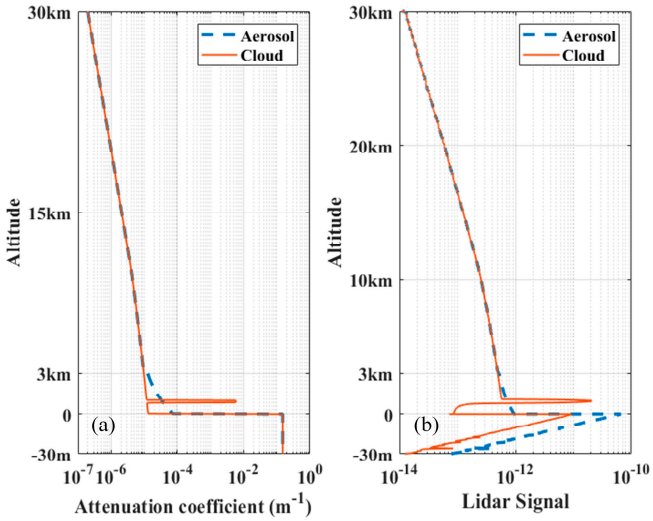


**Figure 6.** (**a**) The optical properties of atmosphere and seawater and (**b**) the spaceborne lidar signal of atmosphere and seawater.

For the aerosol case, the atmosphere within 4 km above the ocean surface is assumed to contain maritime clean aerosols with a relative humidity of 50% called Maritime-50 [40]. The distribution of aerosol particles with height is described as [40]

$$N(h) = N(0)e^{-h} \tag{14}$$

where $h$ is the altitude above the ocean surface. Maritime-50 is composed of three types of aerosol components, including water-soluble, accumulate sea salt (acc.), and coarse sea salt (coa.). The properties of each aerosol component at wavelength of 532 nm are shown in Table 2. The absorption coefficient $a$ and scattering coefficient $b$ are normalized to a number density of 1 particle per $cm^3$. The phase functions of these three aerosols are calculated by the Mie theory which is explained in Section 2.3 with the logarithmic distributions of the particle radius. The values of $r_{mod}$ and $\mu$ used in Equation (9) are shown in Table 2 according to the data given by OPAC [40]. The total values of the $a$, $b$, and phase functions of the mixed aerosol Maritime-50 can be calculated by

$$\begin{cases} a = \sum_i a_i N_i, b = \sum_i b_i N_i \\ \widetilde{\beta}(\theta) = \sum_i \frac{b_i}{b} \widetilde{\beta}_i(\theta) \end{cases} \quad (15)$$

where $a_i$ and $b_i$ are the absorption and scattering coefficients of aerosol component $i$, respectively.

**Table 2.** Optical properties of Maritime-50 aerosol.

| Parameter | Component | | |
|---|---|---|---|
| | **Water Soluble** | **Sea Salt (acc.)** | **Sea Salt (coa.)** |
| $a$ ($m^{-1}$) | $1.4699 \times 10^{-7}$ | $4.2842 \times 10^{-10}$ | $1.749 \times 10^{-7}$ |
| $b$ ($m^{-1}$) | $9.9114 \times 10^{-6}$ | $3.723 \times 10^{-3}$ | 0.218 |
| $N$ ($cm^{-3}$) | 1500 | 20 | $2 \times 10^{-3}$ |
| $r_{mod}$ | 0.0212 | 0.209 | 1.75 |
| $\mu$ | 2.24 | 2.03 | 2.03 |

For the cloud case, the marine cloud with a number density of 50 $cm^{-3}$, droplet sizes of Gamma distribution, and the scattering coefficient of 0.0058 $m^{-1}$ is assumed to be uniformly distributed in an altitude range of 600–800 m. The open ocean water with the IOPs given in Table 3 are used as an example [51]. The Petzold phase function is used in the simulations. The vertical distribution of the optical properties of atmosphere and seawater is shown in Figure 6a. The absorption of aerosol and cloud is weak, so the total attenuation mainly consists of scattering. The attenuation coefficient of the cloud layer is peaked. The lidar return signals from atmosphere and ocean obtained by the simulator are shown in Figure 6b. The vertical resolution of the signal in atmosphere is 30 m with reference to CALIOP [17], and the vertical resolution in seawater is set to 0.3 m. The spaceborne lidar return signal increases with the decreasing altitude because of the increase in the attenuation coefficient of the atmosphere. The lidar signals of the aerosol and cloud layers are much stronger than that of the air molecule. The high attenuation of the cloud layer (with an optical depth of 1.2) causes the lidar signals of the molecule layer under the cloud layer and seawater to be weak. The signal of seawater is much stronger than that of atmosphere because of the high backscattering, and it attenuates quickly because of the high absorption and scattering effects.

**Table 3.** Optical properties of typical seawaters [51].

| Parameter | Water | | |
|---|---|---|---|
| | **Open Ocean** | **Coastal Ocean** | **Turbid Harbor** |
| $a$ ($m^{-1}$) | 0.114 | 0.179 | 0.366 |
| $b$ ($m^{-1}$) | 0.037 | 0.219 | 1.824 |
| $c$ ($m^{-1}$) | 0.151 | 0.398 | 2.190 |

### 3.2. Verification of the Simulator's Accuracy

The normalized lidar signal of seawater obtained by the simulator and theoretical lidar equations are compared to verify the accuracy of the simulator. The atmosphere is set to vacuum, which means

$T_a = 1$ in Equation (1) to simplify the calculation. Three types of seawater (with IOPs shown in Table 3) with the Petzold phase function are used for simulation. The simulation results in Figure 7 (the solid lines) show that the signal attenuation slope is related to the optical properties of the seawater. The signal attenuation slope of the turbid water with a high attenuation coefficient is larger than that of the other two types of seawater.

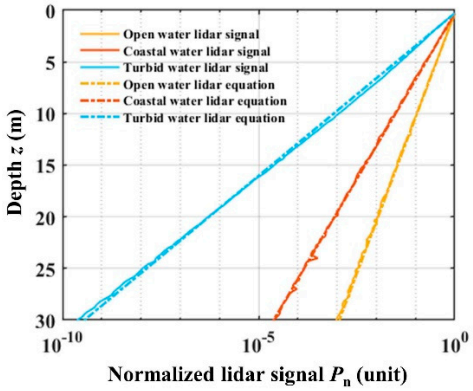


**Figure 7.** The normalized lidar signal with different seawaters obtained by the theoretical equations and the simulator.

The FOV in these simulations is 0.15 mrad, and the height of lidar is 700 km, so the radius of the footprint on the sea surface of the lidar receiving system is about 52.5 m. The effective attenuation coefficient $k_{\text{lidar}}$ is close to the absorption coefficient $a$ of seawater, as explained in Section 2.1. Substituting the relationship $k_{\text{lidar}} \approx a$ into Equation (1) and rewriting it, we have the normalized lidar signal $P_n(z)$ expressed by [19]

$$P_n(z) = \frac{P(z)(nH+z)^2}{P_0 K\left(\frac{v\tau}{2n}\right) A T_a^2 T_s^2 \beta_\pi(z)} \approx \exp(-2az). \tag{16}$$

To verify the accuracy of the simulator, we compare the normalized lidar return signal (dotted lines in Figure 7) with the simulated ones (solid lines in Figure 7) for three typical seawaters. It shows great consistence between the signals calculated by the lidar equation and the simulator, which verifies the accuracy of the simulator. In addition, the multiple scattering effect can be explained further. As the FOV is large enough, the interaction volume of the photon packet is within the FOV of the receiver. The attenuation of the lidar signal is almost caused by absorption without no scattering loss. The receiver can collect all the multiple scattered signals. Thus, the lidar effective attenuation coefficient is very close to the absorption coefficient. For further explanation, we have published a specialized paper about the relationship between the $k_{\text{lidar}}$ value of the spaceborne oceanic lidar signal and the IOPs of case 1 waters under the fully multiple scattering condition [19].

## 4. Discussion

The purposes of this simulator are to obtain the lidar returns and analyze the law of signals under different conditions. Eventually, we will find the optimal lidar system parameters according to detection conditions and apply them to the actual system design. In this section, the lidar signal with different scattering phase functions and inhomogeneous seawaters are simulated and discussed.

### *4.1. Influence of Different Scattering Phase Functions*

This simulator includes four types of oceanic scattering phase functions, as mentioned in Section 2.3. To compare the influence of different phase functions, the lidar return signals of homogeneous coastal ocean waters with four scattering phase functions (Figure 5) are analyzed, and the results are presented

in Figure 8. The lidar signal for water with the TTHG phase function is the strongest because of the higher backscattering probability of the TTHG phase function. According to the phase function in Figure 5, the intensity of the TTHG phase function for the scattering angle near 180° is much stronger than the other three, resulting in a higher lidar return signal. The lidar signal for water with the FF phase function is similar to that for the Petzold phase function. The lidar signal for water with the OTHG phase function near the air–ocean interface is lower, because the value of the HG phase function is the smallest at the scattering angle of 180°. Therefore, the backscattering characteristic of the phase function is the key factor in the lidar signal formation.

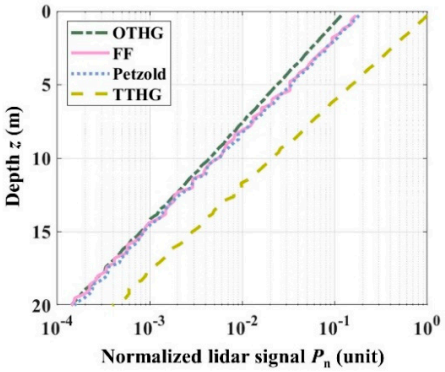


**Figure 8.** Simulation results of different scattering phase functions.

Lidar signals for OTHG, FF, and Petzold phase functions tend to be equal, and the difference between the signal for the TTHG phase function and the other three tends to be small with the increasing depth. The reason for this tendency lies in the multiple scattering effect. The emitted laser beam maintains good collimation in the shallow water, and the backscattering angle is nearly 180°. As the depth increases, the laser beam gradually diverges due to the multiple scattering, resulting in a backscattering angle less than 180° [52]. With the increases of depth, multiple scattering shows stronger impacts on the lidar signal. The backward TTHG phase function decreases with the decrease of the angle, while the other three backward phase functions increase with the decrease of the angle, so that the gap of the signal decreases. More detailed information about the influence of the phase function on the lidar signal is shown in [52].

### *4.2. Lidar Signals from Inhomogeneous Seawaters*

In reality, seawater is normally inhomogeneous, and the IOPs of case 1 water are closely related to the chlorophyll a concentration [Chla]. The vertical distribution of chlorophyll a concentration conforms to the Gaussian distribution given by [53]

$$C(\zeta) = C_b - s\zeta + C_{max} \exp\left\{-\left[(\zeta - \zeta_{max})/\Delta\zeta\right]^2\right\} \quad (17)$$

where $\zeta$ is the dimensionless depth obtained by dividing the geometric depth $z$ by the depth of the euphotic layer, $z_{eu}$, $\zeta = z/z_{eu}$. $C(\zeta) = [\text{Chla}(\zeta)]/\overline{\text{Chla}}_{Zeu}$ is the dimensionless concentration of chlorophyll a, and $\overline{\text{Chla}}_{Zeu}$ is the average concentration of chlorophyll within the euphotic layer. $C_b$ is the background chlorophyll a concentration, which decreases linearly from the surface value $[\text{Chla}]_s$ with the slope $s$. $C_{max}$ is the maximum concentration, $\zeta_{max}$ is the depth of the concentration, and maximum $\Delta\zeta$ represents the width of the peak.

Uitz et al. divided the world's stratified case 1 waters into 9 types (named S1–S9) based on the near-surface chlorophyll a concentration [53]. Three types (S1, S4, and S7 mentioned in reference [53])

of case 1 water are utilized here. The absorption coefficient can be calculated based on the bio-optical model of case 1 water [54]

$$a(\lambda) = [a_w(\lambda) + 0.06a_c^*(\lambda)[\text{Chla}]^{0.65}] \times [1 + 0.2\exp(-0.014(\lambda - 440))] \quad (18)$$

where $a_w(\lambda)$ is the absorption coefficient of pure sea water and $a_c^*(\lambda)$ is a nondimensional statistically derived chlorophyll-specific absorption coefficient. The scattering coefficient is given by [54]

$$b(\lambda) = b_w(\lambda) + (550/\lambda) \times 0.3 \times [\text{Chla}]^{0.62} \quad (19)$$

where $b_w(\lambda)$ is the scattering coefficient of pure seawater, and its value is 0.022 $m^{-1}$ at a wavelength of 532 nm. The vertical distributions of the inherent optical properties (IOPs) and chlorophyll a concentration for these three waters are shown in Figure 9.

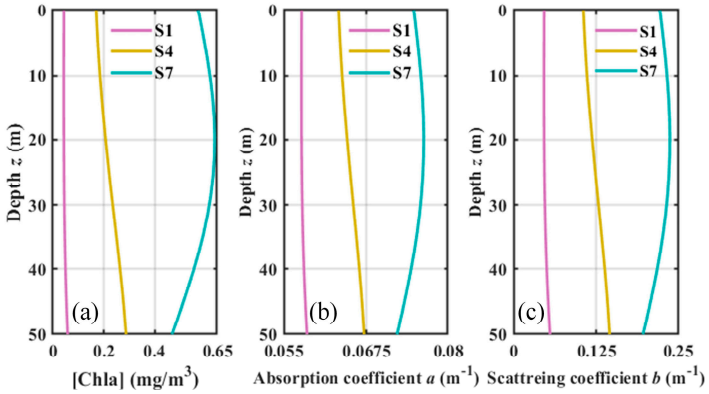


**Figure 9.** The vertical distribution of the chlorophyll a concentration and inherent optical properties (IOPs). (**a**) Concentration of chlorophyll a, (**b**) absorption coefficient, and (**c**) scattering coefficient.

The simulation results of these waters are shown in Figure 10. Different concentrations lead to different optical properties of seawater, which makes different slopes of the lidar signal. The attenuation of the lidar signal is stable, because the optical properties change slowly with depth. These results show that this simulator can be used for inhomogeneous seawater and even for the study of the subsurface scattering layers.

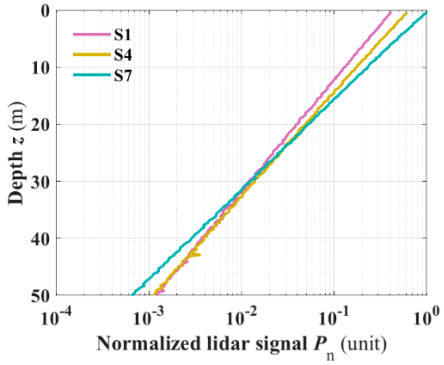


**Figure 10.** Simulation results of the inhomogeneous case 1 waters.

## 5. Conclusions and Outlook

This paper introduces the principle, process, and method of the spaceborne oceanic lidar signal simulator. The simulation model of the lidar signal from the atmosphere and ocean is established for different scattering phase functions and water types, and some preliminary results are presented. We compare the simulated lidar signal with the theoretical lidar equation to verify the accuracy of the

simulator, and the results show great consistency between them. The simulator can get the spaceborne oceanic lidar signals for both homogeneous and inhomogeneous seawaters. The comparisons indicate that the scattering phase function has an obvious impact on the lidar signal, which is consistent with the conclusion about the phase function in reference [52]. The larger the attenuation coefficient, the higher the slope. The effective attenuation coefficient is commonly weaker in the atmosphere than that in the seawater. The relationship between the effective attenuation coefficient and the lidar system including FOV and lidar height is discussed carefully in reference [19]. The comprehensive simulation of the spaceborne oceanic lidar is a very complex project. Although we have achieved some preliminary results so far, this simulator can be further improved in terms of mechanism, performance, efficiency, and so on.

The semianalytical MC method, as the principle of the simulator, also can be used to simulate the polarized lidar and high-spectral resolution lidar (HSRL) signals (not shown here). Liu et al. [32] used the MC method to obtain the polarization lidar signal and compared it with the experimental data, as the polarization characteristics of the lidar signal include the IOPs information of seawater. Zhou et al. [55] developed a semianalytic Monte Carlo model to simulate the HSRL signals with multiple scattering. We are working on the integration of these simulation models for lidars with different mechanisms into the simulator.

In addition, the air–ocean interface is very complex because of the wind, bubble, and foam [13]. The complex sea surface influences the propagation properties of the laser beam and the form of the lidar signal. The air interface in the current simulator is assumed to be flat, and it can be improved to be a wind-roughed one.

Furthermore, when the mechanism and radiation transmission process are complete and complex, the efficiency of the MC method will be a serious limitation. At present, the simulator runs on the Central Processing Unit (CPU), and the simulation speed is slow. A Graphics Processing Unit (GPU) is especially suitable for processing the parallel tracking of multiple independent photons in MC simulation. Erik et al. [56] first proposed a parallel implementation based on the compute unified device architecture (CUDA) running on a GPU, and the speed is 1000 times faster than that of a CPU. Since then, GPU multithreaded parallel computing has gradually been widely used in biomedical optics and passive remote sensing [57,58]. We will apply the GPU acceleration technology into this simulator to improve the simulation efficiency.

The simulator will also be equipped with data calibration and retrieval abilities in the future. The limitation of the hardware parameters such as dynamic range should be considered in practical applications. We will also evaluate the actual parameters of the spaceborne oceanic lidar system, which is conducive to the design of the future spaceborne oceanic lidar system. In addition, through the simulation of various lidar signal models, a complete inversion algorithm is attempted to be established to obtain the IOPs of the seawater, which can be compared with the data of CALIOP to continuously improve the performance of the simulator [35,48], which is of great significance for global biomass and carbon stock estimation.

**Author Contributions:** Conceptualization, Q.L. and D.L.; methodology, Q.L. and X.C.; software execution, X.C. and J.B.; investigation, C.J., X.Z., Z.M. and P.C.; writing—original draft preparation, Q.L. and X.C.; writing—review and editing, Q.L.; supervision, D.L.; funding acquisition, D.L. All authors have read and agreed to the published version of the manuscript.

**Funding:** This work received partial financial support from the National Key Research and Development Program of China (2016YFC1400900); National Natural Science Foundation of China (41775023); Excellent Young Scientist Program of Zhejiang Provincial Natural Science of China (LR19D050001); Fundamental Research Funds for the Central Universities (2019FZJD011); State Key Laboratory of Modern Optical Instrumentation Innovation Program.

**Conflicts of Interest:** The authors declare no conflict of interest. The funders had no role in the design of the study; in the collection, analyses, or interpretation of data; in the writing of the manuscript, or in the decision to publish the results.

## References


1. Revelamarche, A.; Alvain, S.; Racault, M.; Dessailly, D.; Guiselin, N.; Jamet, C.; Vantrepotte, V.; Beaugrand, G. Estimation of the Potential Detection of Diatom Assemblages Based on Ocean Color Radiance Anomalies in the North Sea. *Front. Mar. Sci.* **2017**, *4*, 408. [CrossRef]
2. Vedernikov, V.I.; Gagarin, V.I.; Demidov, A.B.; Burenkov, V.I.; Stunzhas, P.A. Primary production and chlorophyll distributions in the subtropical and tropical waters of the Atlantic Ocean in the autumn of 2002. *Oceanology* **2007**, *47*, 386–399. [CrossRef]
3. Kulk, G.; Platt, T.; Dingle, J.; Jackson, T.; Jonsson, B.F.; Bouman, H.A.; Babin, M.; Brewin, R.J.W.; Doblin, M.; Estrada, M.; et al. Primary Production, an Index of Climate Change in the Ocean: Satellite-Based Estimates over Two Decades. *Remote Sens.* **2020**, *12*, 826. [CrossRef]
4. Sosik, H.M. Characterizing seawater constituents from optical properties. In *Real-Time Coastal Observing Systems for Ecosystem Dynamics and Harmful Algal Blooms*; UNESCO: Paris, France, 2008.
5. Mcclain, C.R. A Decade of Satellite Ocean Color Observations*. *Annu. Rev. Mar. Sci.* **2009**, *1*, 19. [CrossRef]
6. Werdell, P.J.; McKinna, L.I.W.; Boss, E.; Ackleson, S.G.; Craig, S.E.; Gregg, W.W.; Lee, Z.; Maritorena, S.; Roesler, C.S.; Rousseaux, C.S. An overview of approaches and challenges for retrieving marine inherent optical properties from ocean color remote sensing. *Prog. Oceanogr.* **2018**, *160*, 186–212. [CrossRef]
7. Hostetler, C.A.; Behrenfeld, M.J.; Hu, Y.; Hair, J.W.; Schulien, J.A. Spaceborne Lidar in the Study of Marine Systems. *Annu. Rev. Mar. Sci.* **2017**, *10*. [CrossRef]
8. Churnside, J.H. Review of profiling oceanographic lidar. *Opt. Eng.* **2014**, *53*, 051405. [CrossRef]
9. Jamet, C.; Mj, B.; Ab, D.; Ov, K.; Gilerson, A. Going Beyond Standard Ocean Color Observations: Lidar and Polarimetry. *Front. Mar. Sci.* **2019**, *6*, 251. [CrossRef]
10. Liu, D.; Xu, P.; Zhou, Y.; Chen, W.; Han, B.; Zhu, X.; He, Y.; Mao, Z.; Le, C.; Chen, P. Lidar Remote Sensing of Seawater Optical Properties: Experiment and Monte Carlo Simulation. *IEEE Trans. Geosci. Remote Sens.* **2019**, *57*, 9489–9498. [CrossRef]
11. Churnside, J.H. LIDAR detection of plankton in the ocean. In Proceedings of the IEEE International Geoscience and Remote Sensing Symposium, Barcelona, Spain, 23–28 July 2007; pp. 3174–3177.
12. Churnside, J.H.; Wilson, J.J.; Tatarskii, V.V. Airborne lidar for fisheries applications. *Opt. Eng.* **2001**, *40*, 406–414. [CrossRef]
13. Liu, Q.; Liu, D.; Bai, J.; Zhang, Y.; Shen, X. Influence of ocean surface waves and air bubbles on the polarization characteristics of spaceborne oceanographic lidar returns. In Proceedings of the Remote Sensing of the Ocean, Sea Ice, Coastal Waters, and Large Water Regions 2018, Berlin, Germany, 10–12 September 2018.
14. Churnside, J.H.; Ostrovsky, L.A. Lidar observation of a strongly nonlinear internal wave train in the Gulf of Alaska. *Int. J. Remote Sens.* **2005**, *26*, 167–177. [CrossRef]
15. Collister, B.L.; Zimmerman, R.C.; Sukenik, C.I.; Hill, V.J.; Balch, W.M. Remote sensing of optical characteristics and particle distributions of the upper ocean using shipboard lidar. *Remote Sens. Environ.* **2018**, *215*, 85–96. [CrossRef]
16. Chen, P.; Pan, D.L. Ocean Optical Profiling in South China Sea Using Airborne LiDAR. *Remote Sens.* **2019**, *11*, 1826. [CrossRef]
17. Winker, D.M.; Vaughan, M.A.; Omar, A.; Hu, Y.; Powell, K.A.; Liu, Z.; Hunt, W.H.; Young, S.A. Overview of the CALIPSO mission and CALIOP data processing algorithms. *J. Atmos. Ocean. Technol.* **2009**, *26*, 2310–2323. [CrossRef]
18. Hu, Y. Ocean, Land and Meteorology Studies Using Space-Based Lidar Measurements. In Proceedings of the 5th WSEAS Internatinal Conference on Remote Sensing, Washington, DC, USA, 17–19 October 2009.
19. Liu, Q.; Liu, D.; Bai, J.; Zhang, Y.; Zhou, Y.; Xu, P.; Liu, Z.; Chen, S.; Che, H.; Wu, L.; et al. Relationship between the effective attenuation coefficient of spaceborne lidar signal and the IOPs of seawater. *Opt. Express* **2018**, *26*, 30278–30291. [CrossRef]
20. Markus, T.; Neumann, T.; Martino, A.; Abdalati, W.; Brunt, K.; Csatho, B.; Farrell, S.; Fricker, H.; Gardner, A.; Harding, D.; et al. The Ice, Cloud, and land Elevation Satellite-2 (ICESat-2): Science requirements, concept, and implementation. *Remote Sens. Environ.* **2017**, *190*, 260–273. [CrossRef]
21. Lolli, S.; Delaval, A.; Loth, C.; Garnier, A.; Flamant, P.H. 0.355-micrometer direct detection wind lidar under testing during a field campaign in consideration of ESA's ADM-Aeolus mission. *Atmos. Meas. Tech.* **2013**, *6*, 3349–3358. [CrossRef]

22. Kanitz, T.; Lochard, J.; Marshall, J.; McGoldrick, P.; Lecrenier, O.; Bravetti, P.; Reitebuch, O.; Rennie, M.; Wernham, D.; Elfving, A. Aeolus First Light—First Glimpse. In Proceedings of the International Conference on Space Optics-ICSO 2018, Chania, Greece, 9–12 October 2018; Sodnick, Z., Karafolas, N., Cugny, B., Eds.; International Society for Optics and Photonics: Bellingham, WA, USA, 2018; Volume 11180.
23. Chen, G.; Tang, J.; Zhao, C.; Wu, S.; Yu, F.; Ma, C.; Xu, Y.; Chen, W.; Zhang, Y.; Liu, J. Concept Design of the "Guanlan" Science Mission: China's Novel Contribution to Space Oceanography. *Front. Mar. Sci.* **2019**, *6*, 194. [CrossRef]
24. Abdallah, H.; Baghdadi, N.; Bailly, J.-S.; Pastol, Y.; Fabre, F. Wa-LiD: A new LiDAR simulator for waters. *IEEE Geosci. Remote Sens. Lett.* **2012**, *9*, 744–748. [CrossRef]
25. Walker, R.E.; Mclean, J.W. Lidar equations for turbid media with pulse stretching. *Appl. Opt.* **1999**, *38*, 2384–2397. [CrossRef] [PubMed]
26. Poole, L.R.; Venable, D.D.; Campbell, J.W. Semianalytic Monte Carlo radiative transfer model for oceanographic lidar systems. *Appl. Opt.* **1981**, *20*, 3653–3656. [CrossRef] [PubMed]
27. Punjabi, A.; Venable, D.D. Effects of multiple scattering on time- and depth-resolved signals in airborne lidar systems. *Int. J. Remote Sens.* **1986**, *7*, 615–626. [CrossRef]
28. Gordon, H.R. Interpretation of airborne oceanic lidar: Effects of multiple scattering. *Appl. Opt.* **1982**, *21*, 2996–3001. [CrossRef]
29. Zaccanti, G.; Bruscaglioni, P.; Dami, M. Simple inexpensive method of measuring the temporal spreading of a light pulse propagating in a turbid medium. *Appl. Opt.* **1990**, *29*, 3938–3944. [CrossRef] [PubMed]
30. Bissonnette, L.R. Multiple-scattering lidar equation. *Appl. Opt.* **1996**, *35*, 6449–6465. [CrossRef] [PubMed]
31. Zhou, Y.; Chen, W.; Cui, X.; Malinka, A.; Liu, Q.; Han, B.; Wang, X.; Zhuo, W.; Che, H.; Song, Q.; et al. Validation of the Analytical Model of Oceanic Lidar Returns: Comparisons with Monte Carlo Simulations and Experimental Results. *Remote Sens.* **2019**, *11*, 1870. [CrossRef]
32. Liu, Q.; Cui, X.; Chen, W.; Liu, C.; Bai, J.; Zhang, Y.; Zhou, Y.; Liu, Z.; Xu, P.; Che, H.; et al. A semianalytic Monte Carlo radiative transfer model for polarized oceanic lidar: Experiment-based comparisons and multiple scattering effects analyses. *J. Quant. Spectrosc. Radiat. Transf.* **2019**, *237*, 106638. [CrossRef]
33. Zaccanti, G.; Bruscaglioni, P.; Gurioli, M.; Sansoni, P. Laboratory Simulations of Lidar Returns from Clouds—Experimental and Numerical Results. *Appl. Opt.* **1993**, *32*, 1590–1597. [CrossRef]
34. Behrenfeld, M.J.; Hu, Y.; O'Malley, R.T.; Boss, E.S.; Hostetler, C.A.; Siegel, D.A.; Sarmiento, J.L.; Schulien, J.; Hair, J.W.; Lu, X. Annual boom-bust cycles of polar phytoplankton biomass revealed by space-based lidar. *Nat. Geosci.* **2016**, *10*, 118–122. [CrossRef]
35. Behrenfeld, M.J.; Hu, Y.; Hostetler, C.A.; Dall'Olmo, G.; Rodier, S.D.; Hair, J.W.; Trepte, C.R. Space-based lidar measurements of global ocean carbon stocks. *Geophys. Res. Lett.* **2013**, *40*, 4355–4360. [CrossRef]
36. Phillips, D.; Koerber, B. A Theoretical Study of an Airborne Laser Technique for determining Sea Water Turbidity. *Aust. J. Phys.* **1984**, *37*, 75. [CrossRef]
37. Cui, X.; Liu, Q.; Zhou, Y.; Zhang, K.; Liu, D. Program of spaceborne oceanic lidar based on semianalytic monte carlo method. In Proceedings of the 2019 Photonics and Electromagnetics Research Symposium—Fall, PIERS—Fall 2019, Xiamen, China, 17–20 December 2019; pp. 919–927.
38. Morel, A. Optical properties of pure water and pure sea water. *Opt. Asp. Oceanogr.* **1974**, *1*, 1–24.
39. Liou, K.-N. A complementary theory of light scattering by homogeneous spheres. *Appl. Math. Comput.* **1977**, *3*, 331–358. [CrossRef]
40. Hess, M.; Koepke, P.; Schult, I. Optical properties of aerosols and clouds: The software package OPAC. *Bull. Am. Meteorol. Soc.* **1998**, *79*, 831–844. [CrossRef]
41. Petzold, T.J. *Volume Scattering Functions for Selected Ocean Waters*; Scripps Institution of Oceanography La Jolla Ca Visibility Lab: San Diego, CA, USA, 1972.
42. Henyey, L.G.; Greenstein, J.L. Diffuse radiation in the Galaxy. *Astrophys. J.* **1941**, *93*, 70–83. [CrossRef]
43. Kattawar, G.W. A three-parameter analytic phase function for multiple scattering calculations. *J. Quant. Spectrosc. Radiat. Transf.* **1975**, *15*, 839–849. [CrossRef]
44. Haltrin, V.I. One-parameter two-term Henyey-Greenstein phase function for light scattering in seawater. *Appl. Opt.* **2002**, *41*, 1022–1028. [CrossRef]
45. Fournier, G.R.; Forand, J.L. Analytic phase function for ocean water. In Proceedings of the SPIE—The International Society for Optical Engineering, Bergen, Norway, 13–15 June 1994; Volume 2258, pp. 194–201.

46. Mobley, C.D.; Sundman, L.K.; Boss, E. Phase function effects on oceanic light fields. *Appl. Opt.* **2002**, *41*, 1035–1050. [CrossRef]
47. Fournier, G.R.; Jonasz, M. Computer based underwater imaging analysis. In *Airborne and In-Water Underwater Imaging*; Gilbert, G.D., Ed.; Spie-Int Soc Optical Engineering: Bellingham, WA, USA, 1999; Volume 3761, pp. 62–70.
48. Lu, X.; Hu, Y.; Trepte, C.; Zeng, S.; Churnside, J.H. Ocean subsurface studies with the CALIPSO spaceborne lidar. *J. Geophys. Res. Ocean.* **2014**, *119*, 4305–4317. [CrossRef]
49. Lu, X.; Hu, Y.; Pelon, J.; Trepte, C.; Liu, K.; Rodier, S.; Zeng, S.; Lucker, P.; Verhappen, R.; Wilson, J. Retrieval of ocean subsurface particulate backscattering coefficient from space-borne CALIOP lidar measurements. *Opt. Express* **2016**, *24*, 29001. [CrossRef]
50. Bucholtz, A. Rayleigh-Scattering Calculations for the Terrestrial Atmosphere. *Appl. Opt.* **1995**, *34*, 2765–2773. [CrossRef] [PubMed]
51. Mobley, C.D. *Light and Water: Radiative Transfer in Natural Waters*; Academic Press: Cambridge, MA, USA, 1994.
52. Liu, D.; Zhou, Y.; Chen, W.; Liu, Q.; Huang, T.; Liu, W.; Chen, Q.; Liu, Z.; Xu, P.; Cui, X.; et al. Phase function effects on the retrieval of oceanic high-spectral-resolution lidar. *Opt. Express* **2019**, *27*, A654–A668. [CrossRef] [PubMed]
53. Uitz, J.; Claustre, H.; Morel, A.; Hooker, S.B. Vertical distribution of phytoplankton communities in open ocean: An assessment based on surface chlorophyll. *J. Geophys. Res. Ocean.* **2006**, *111*. [CrossRef]
54. Morel, A. Light and marine photosynthesis: A spectral model with geochemical and climatological implications. *Prog. Oceanogr.* **1991**, *26*, 263–306. [CrossRef]
55. Zhou, Y.; Liu, D.; Xu, P.; Liu, C.; Bai, J.; Yang, L.; Cheng, Z.; Tang, P.; Zhang, Y.; Su, L. Retrieving the seawater volume scattering function at the 180° scattering angle with a high-spectral-resolution lidar. *Opt. Express* **2017**, *25*, 11813–11826. [CrossRef] [PubMed]
56. Alerstam, E.; Svensson, T.; Andersson-Engels, S. Parallel computing with graphics processing units for high-speed Monte Carlo simulation of photon migration. *J. Biomed. Opt.* **2008**, *13*, 060504. [CrossRef]
57. Zhu, C.; Liu, Q. Review of Monte Carlo modeling of light transport in tissues. *J. Biomed. Opt.* **2013**, *18*, 050902. [CrossRef]
58. Ramon, D.; Steinmetz, F.; Jolivet, D.; Compiègne, M.; Frouin, R. Modeling polarized radiative transfer in the ocean-atmosphere system with the GPU-accelerated SMART-G Monte Carlo code. *J. Quant. Spectrosc. Radiat. Transf.* **2019**, *222*, 89–107. [CrossRef]